Обзор ArXiv: astro-ph, 15-19 апреля 2019 года

От Сильченко О.К.

ArXiv: 1904.07246

Revealing Dust Obscured Star Formation in CLJ1449+0856, a Cluster at z=2

C. M. A. Smith,[1]⋆ W. K. Gear,[1] M. W. L. Smith,[1] A. Papageorgiou,[1]
S. A. Eales[1]
[1] *School of Physics and Astronomy, Cardiff University, Queens Building, The Parade, Cardiff, CF24 3AA, UK*

Accepted XXX. Received YYY; in original form ZZZ

ABSTRACT

We present SCUBA-2 450 μm and 850 μm data of the mature redshift 2 cluster CLJ1449. We combine this with archival *Herschel* data to explore the star forming properties of CLJ1449. Using high resolution ALMA and JVLA data we identify potentially confused galaxies, and use the Bayesian inference tool XID+ to estimate fluxes for them. Using archival optical and near infrared data with the energy-balance code CIGALE we calculate star formation rates, and stellar masses for all our cluster members, and find the star formation rate varies between 20-1600 $M_{\odot}yr^{-1}$ over the entire 3 Mpc radial range. The central 0.5 Mpc region itself has a total star formation rate of $800 \pm 200\, M_{\odot}yr^{-1}$, which corresponds to a star formation rate density of $(1.2 \pm 0.3) \times 10^4\, M_{\odot}yr^{-1}Mpc^{-3}$, which is approximately five orders of magnitude greater than expected field values. When comparing this cluster to those at lower redshifts we find that there is an increase in star formation rate per unit volume towards the

Настоящее скопление галактик на z=2

CL J1449+0856 (hereafter CLJ1449, RA= 222.3083 Dec=8.9392) is one of the highest redshift, fully virialized, mature X-ray emitting clusters known. The cluster was first identified as an over-density of red galaxies during *Spitzer* observations of the so called 'Daddi fields' (Daddi et al. 2000). Optical, NIR and X-ray follow ups confirmed this was indeed fully virialised (Kong et al. 2006, Gobat et al. 2011). Follow up spectroscopy confirmed the redshift of the cluster to be z = 1.99, making it one of the most distant clusters discovered (Gobat et al. 2013). The mass of this cluster (derived from the X-ray luminosity - mass correlation) was estimated to be $\sim 5 \times 10^{13} M_{\odot}$ making it a relatively low mass cluster, and a typical progenitor to clusters seen today (Gobat et al. 2011).

32 субмиллиметровых галактик в поле скопления

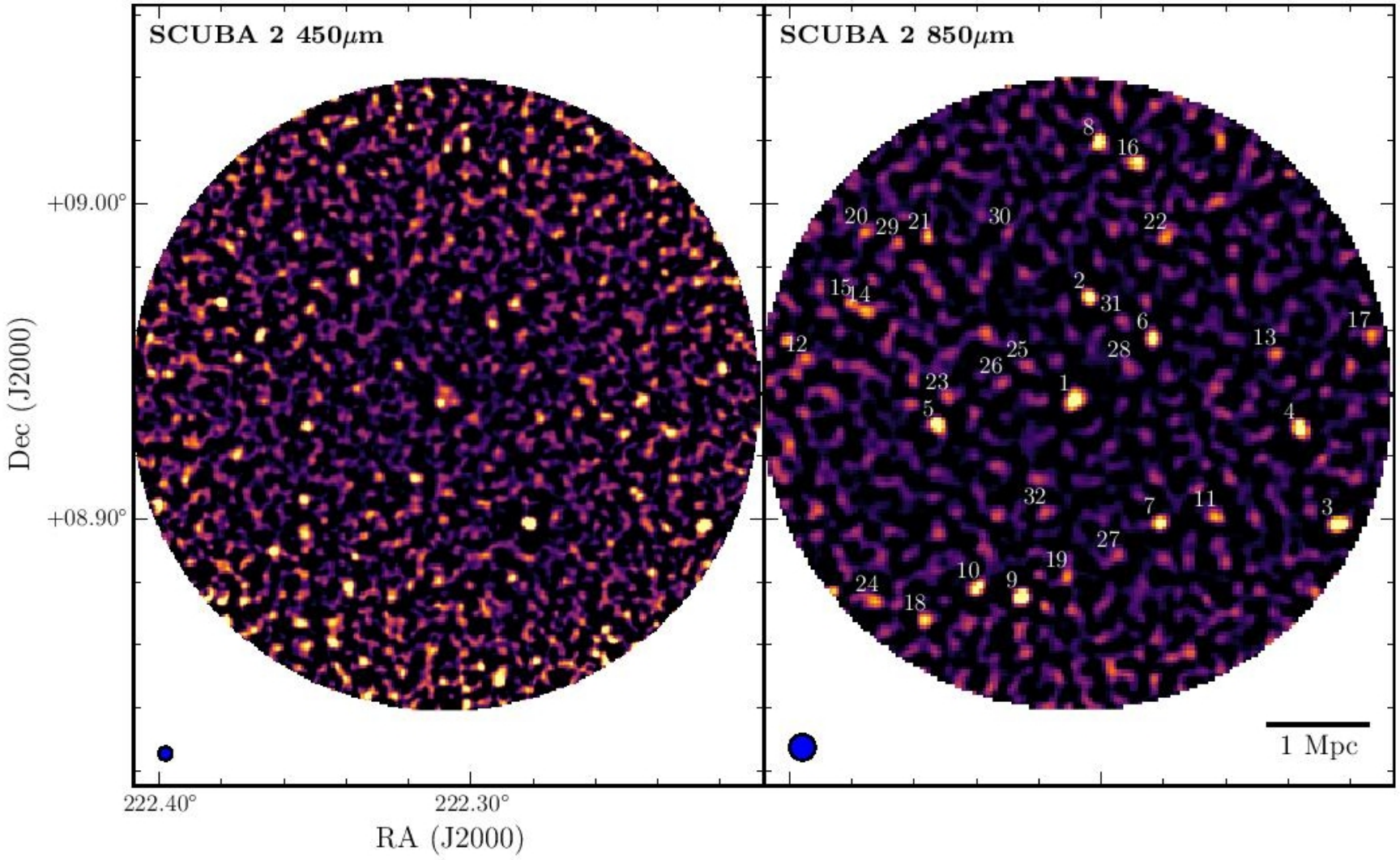

Figure 1. The SCUBA-2 maps of CLJ1449 with a radius of 3 Mpc. The FWHM size of the PSF can be found in the lower left corner.

Центр скопления сняли с ALMA

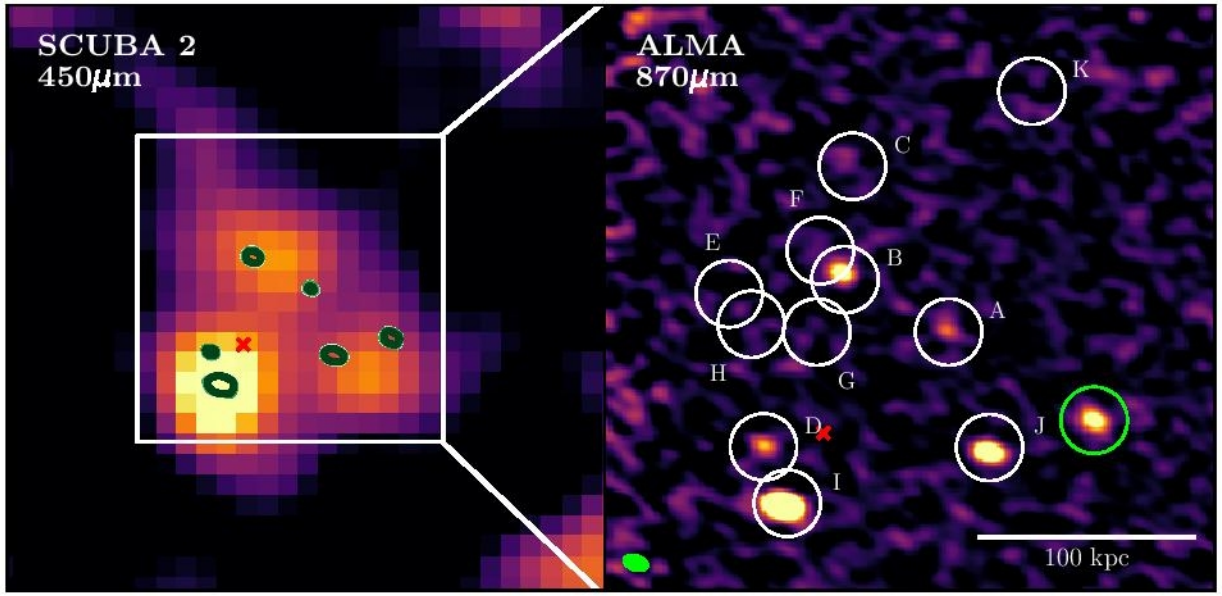

Figure 3. The ALMA 870 μm continuum map of the core of the cluster. The ALMA data resolves the SCUBA-2 450 μm map into 6 individual sources rather then 3. The size of the PSF can be see in the bottom left corner. The letter represents the sources in Table 3, and are based on the designations from C18. A low redshift object is known to contaminate the cluster, and is illustrated by the green circle. The red cross represents the centre of the x-ray emission from Gobat et al. 2011.

Большая часть красных смещений - фотометрическая

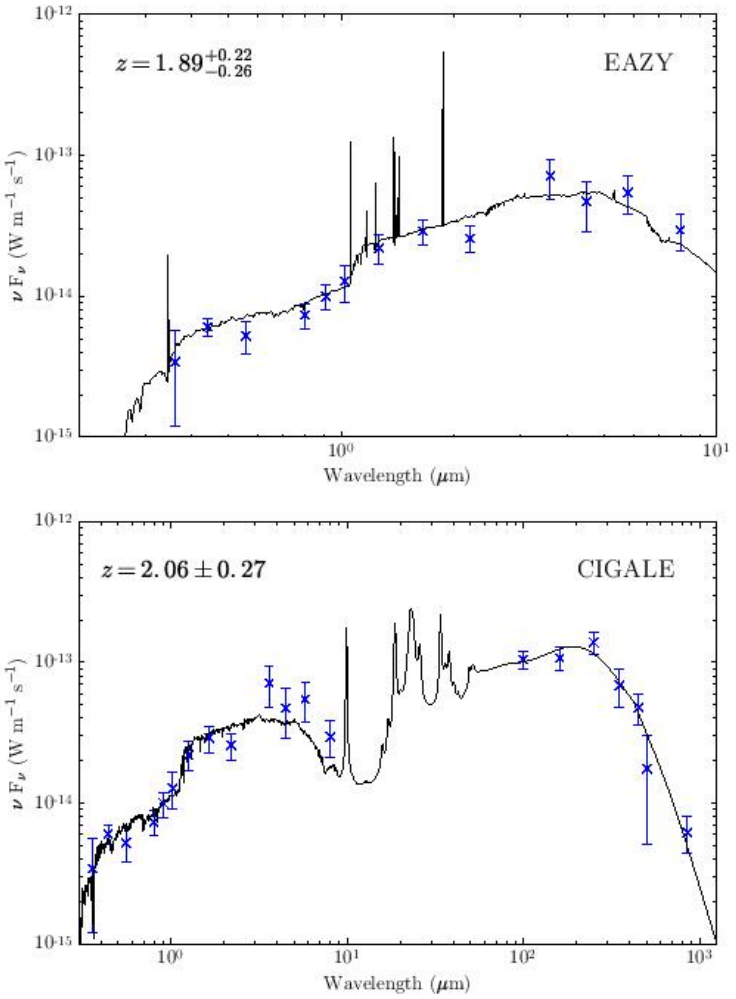

Figure 4. Both the EAZY SED (top) and CIGALE SED (bot-

Результаты

ID	z_{Spec}	z_{EZ}	z_{CG}	L_{IR} (10^{12} $L_\odot$)	SFR ($M_\odot yr^{-1}$)	M_* (10^{11} $M_\odot$)	P
850_1_A	1.9951 ± 0.0004	$2.33^{+0.34}_{-0.31}$	2.25 ± 0.25	0.21 ± 0.15	32 ± 17	0.16 ± 0.08	-
850_1_B	1.9902 ± 0.0005	$2.25^{+0.53}_{-0.55}$	2.14 ± 0.37	0.18 ± 0.22	22 ± 28	0.17 ± 0.21	-
850_1_C	1.9944 ± 0.0006	$2.51^{+0.64}_{-0.87}$	1.92 ± 0.52	0.62 ± 0.38	74 ± 59	0.36 ± 0.17	-
850_1_D	1.9832 ± 0.0007	$2.35^{+0.32}_{-0.28}$	1.70 ± 0.54	0.38 ± 0.10	36 ± 13	0.43 ± 0.13	-
850_1_E	1.9965 ± 0.0004	$3.45^{+0.79}_{-0.70}$	2.23 ± 1.03	0.52 ± 0.48	66 ± 69	0.26 ± 0.37	-
850_1_F	1.9883 ± 0.0070	$1.64^{+0.62}_{-0.66}$	2.02 ± 0.30	0.37 ± 0.30	45 ± 49	0.41 ± 0.22	-
850_1_G	1.9903 ±0.0004	$1.82^{+0.39}_{-0.47}$	1.59 ± 0.37	0.41 ± 0.37	59 ± 67	0.30 ± 0.29	-
850_1_H	1.982 ± 0.002	$2.43^{+0.24}_{-0.24}$	3.62 ± 0.60	0.56 ± 0.67	73 ± 100	0.26 ± 0.44	-
850_1_K	1.98 ± 0.02	$1.24^{+1.20}_{-0.83}$	1.63 ± 0.58	0.30 ± 0.11	37 ± 16	0.30 ± 0.12	-
850_13	-	$1.98^{+0.44}_{-0.47}$	2.25 ± 0.24	0.94 ± 0.23	116 ± 22	2.08 ± 0.53	0.04
850_14	-	$2.10^{+0.42}_{-0.47}$	1.79 ± 0.24	3.03 ± 0.36	331 ± 88	4.09 ± 0.99	0.01
850_17	-	$2.34^{+0.87}_{-0.93}$	1.98 ± 0.40	3.65 ± 1.16	447 ± 156	3.86 ± 1.18	0.04
850_20	-	$2.07^{+0.52}_{-0.51}$	2.04 ± 0.21	4.98 ± 0.38	439 ± 98	6.84 ± 1.48	0.08
850_22	-	$2.35^{+0.43}_{-0.46}$	2.04 ± 0.32	3.30 ± 1.85	403 ± 214	2.28 ± 1.12	0.01
850_25	-	$1.89^{+0.22}_{-0.26}$	2.06 ± 0.27	2.46 ± 0.44	254 ± 71	2.99 ± 0.83	0.01
850_31	-	$2.18^{+0.77}_{-0.68}$	2.17 ± 0.32	2.73 ± 0.41	377 ± 117	1.33 ± 0.56	0.08
850_16	-	$2.34^{+0.58}_{-0.57}$	1.56 ± 0.21	11.64 ± 2.71	1618 ± 738	7.25 ± 6.19	0.01
850_26	-	$1.90^{+1.14}_{-0.86}$	1.26 ± 0.36	2.35 ± 0.98	313 ± 160	0.74 ± 0.52	0.09
850_4	-	$1.56^{+0.92}_{-0.97}$	1.96 ± 0.34	0.93 ± 0.18	105 ± 30	0.58 ± 0.39	0.002
850_5	-	$1.46^{+0.87}_{-0.78}$	1.98 ± 0.70	1.26 ± 0.14	142 ± 40	0.61 ± 0.32	0.004
850_8	-	$1.58^{+0.49}_{-0.41}$	2.10 ± 0.97	1.71 ± 0.28	195 ± 63	0.74 ± 0.49	0.01
850_9	-	$3.52^{+0.35}_{-0.36}$	2.07 ± 0.39	3.55 ± 0.27	357 ± 86	2.51 ± 1.22	0.002
850_24	-	$2.61^{+0.60}_{-0.56}$	2.27 ± 0.39	2.99 ± 0.34	360 ± 101	1.67 ± 0.64	0.01
850_1_J	-	$4.33^{+1.29}_{-1.35}$	1.98 ± 0.43	2.98 ± 0.28	381 ± 138	1.31 ± 1.33	-

Звездообразование в скоплении – выше среднекосмического

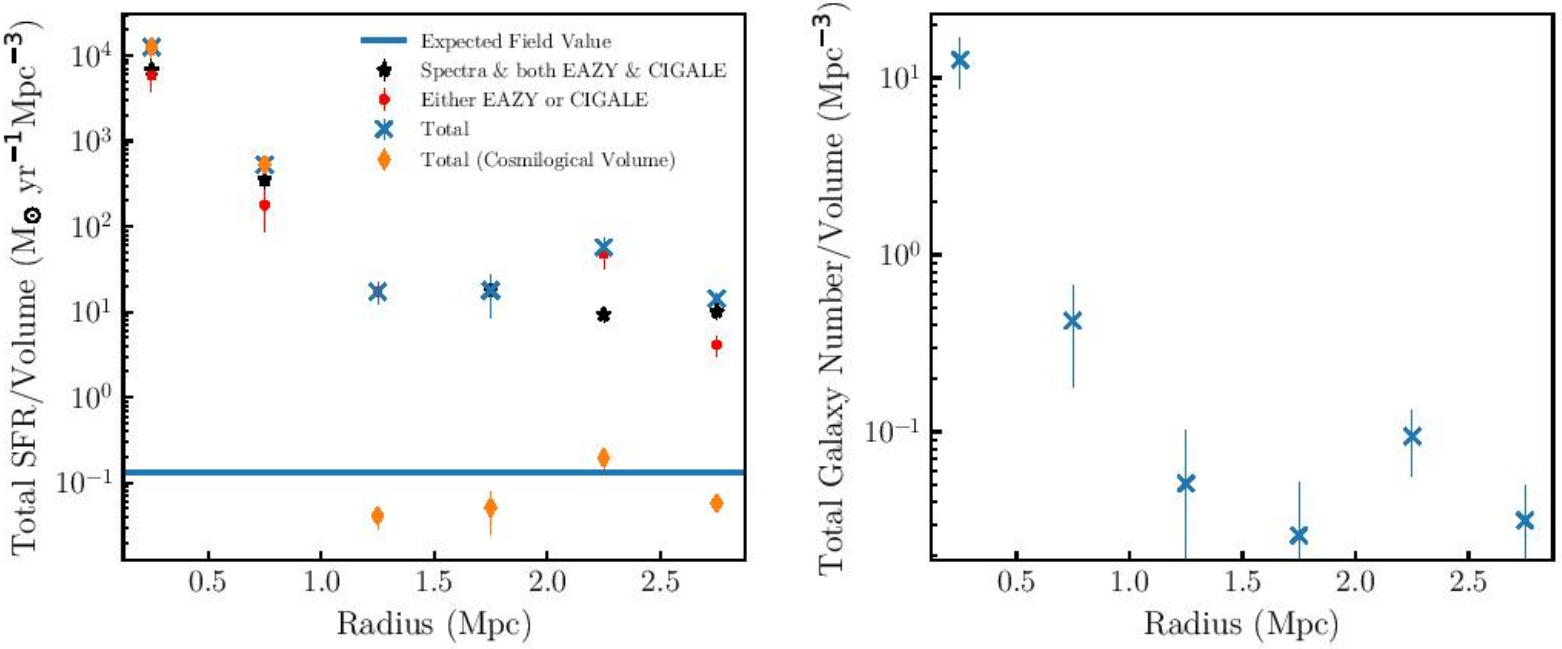

Figure 9. Left: The SF-density relation found in CLJ1449. We have divided the cluster into 0.5 Mpc bins, normalised by the volume of the bin. Each bin has been separated by the redshift criteria mentioned in Section 4. The blue line is the expected field value based on Madau & Dickinson (2014). We also plot the SF-density relation by assuming the observed cosmological volume between 1.6 <z <2.4. Right: The number density of galaxies versus the cluster radius. For sources less than 1 Mpc the counts are from ALMA, whilst at larger radii we use radio counts

Намек на вспышки на средних расстояниях от центра скопления?

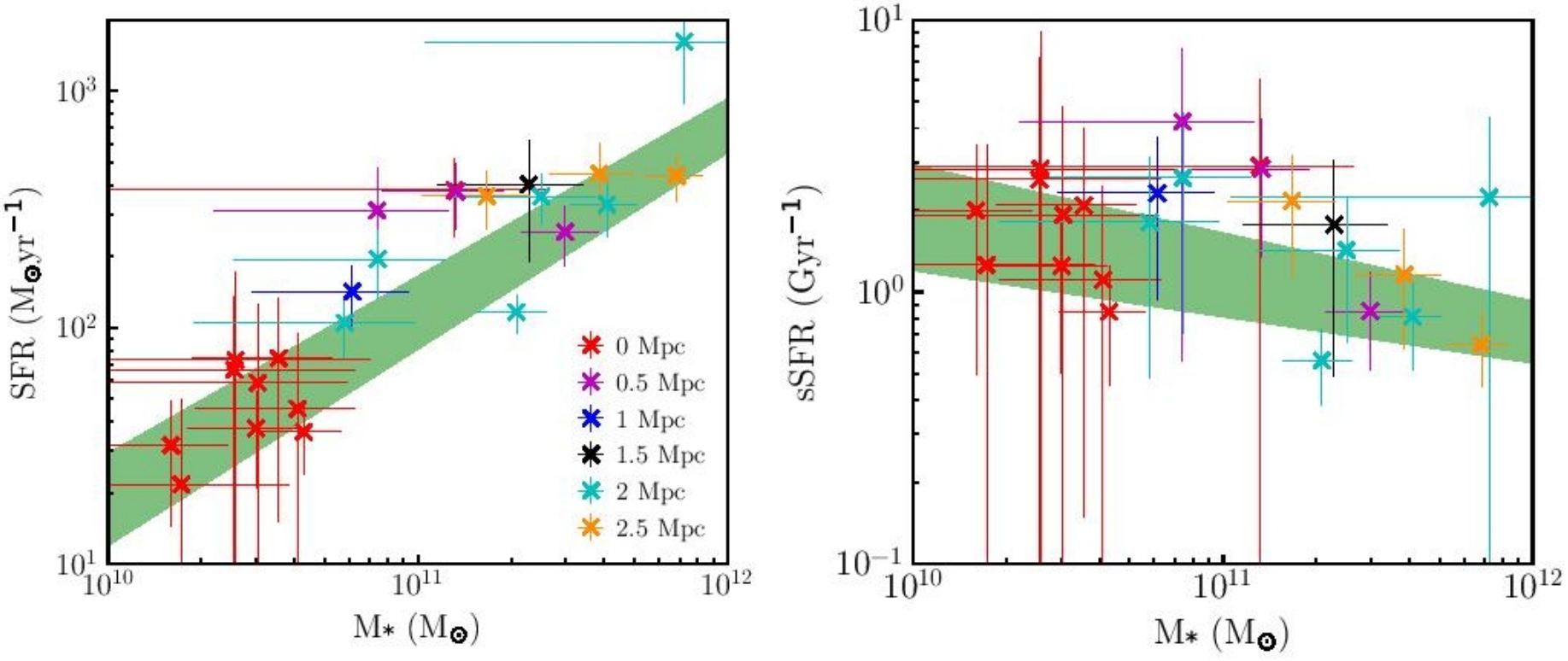

Figure 10. Left: The SFR-M_* relation with the shaded region showing the expected position for main sequence galaxies at redshift 2 given by Sargent et al. (2014). We have divided the points up into there location within the cluster and colour coded them accordingly. Right: The sSFR-M_* relation with the expected value for redshift 2 main sequence galaxies.

Монотонная (и сильная) зависимость темпов SFв скоплениях от z

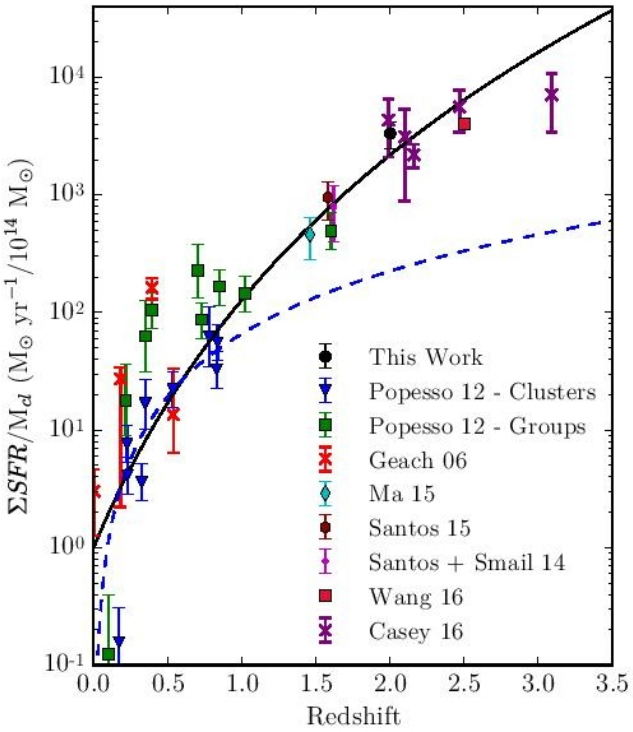

Figure 11. Comparison of the mass normalised ΣSFR for several clusters at different redshifts. The solid black line is the proposed relation offered by Cowie et al. (2004) and Geach et al. (2006) that follows the relation $(1+z)^7$, and the blue dashed line follows the relation in Popesso et al. (2012) for clusters. It should be noted that the sample from Casey (2016) are proto-clusters and

ArXiv: 1904.07880

A flat trend of star-formation rate with X-ray luminosity of galaxies hosting AGN in the SCUBA-2 Cosmology Legacy Survey

Joanna Ramasawmy,[1⋆] Jason Stevens,[1] Garreth Martin[1] and James E. Geach[1]
[1] *Centre for Astrophysics Research, School of Physics, Astronomy and Mathematics, University of Hertfordshire, College Lane, Hatfield AL10 9AB, UK*

Accepted 2019 April 11. Received 2019 April 9; in original form 2019 January 31

ABSTRACT

Feedback processes from active galactic nuclei (AGN) are thought to play a crucial role in regulating star formation in massive galaxies. Previous studies using *Herschel* have resulted in conflicting conclusions as to whether star formation is quenched, enhanced, or not affected by AGN feedback. We use new deep 850 μm observations from the SCUBA-2 Cosmology Legacy survey (S2CLS) to investigate star formation in a sample of X-ray selected AGN, probing galaxies up to $L_{0.5-7\ \mathrm{keV}} = 10^{46}$ erg s^{-1}. Here we present the results of our analysis on a sample of 1957 galaxies at $1 < z < 3$, using both S2CLS and ancilliary data at seven additional wavelengths (24–500 μm) from *Herschel* and *Spitzer*. We perform a stacking analysis, binning our sample by redshift

В нескольких хорошо изученных площадках выбраны рентгеновские источники

Table 1. Properties of the S2CLS fields and X-ray catalogues used to create the sample. Columns list the name of the survey field, the area coverage of the S2CLS data, the 1σ 850 μm depth Geach et al. (2017), the area coverage of the X-ray data, the exposure time of the X-ray data, the sensitivity of the X-ray data, the number of X-ray detected sources across the whole catalogue, the number of X-ray detected sources within the X-ray luminosity and redshift ranges of interest (see 2.2). Note that the deep CDFS X-ray survey lies within the sky area of the shallower E-CDFS field, and thus we combine these catalogues; numbers quoted are those in the combined CDFS/E-CDFS field. Submillimetre data for this CDFS/E-CDFS field are from the LABOCA survey at 870 μm. Catalogue references are given below the table, including those for spectroscopic redshifts.

Field	850 μm area (deg^2)	1σ 850 μm depth (mJy $beam^{-1}$)	X-ray area (deg^2)	X-ray exposure (ks)	X-ray sensitivity (erg $cm^{-2}s^{-1}$)	No. sources [1]	No. sources in L_X, z
Akari-NEP	0.6	1.2	0.34	300	1×10^{-15}	26	6
COSMOS	2.22	1.6	2.2	160	2×10^{-16}	2287	1118
GOODS-N	0.07	1.1	0.13	2000	1.2×10^{-17}	396	74
EGS	0.32	1.2	0.29	800	3.3×10^{-17}	630	205
CDFS	-	-	0.13	7000	1.9×10^{-17}	-	-
E-CDFS	0.25	1.6	0.3	228	1.9×10^{-16}	867	220
UDS	0.96	0.9	1.3	100	3.0×10^{-15}	586	334

[1] Akari-NEP catalogues from Krumpe et al. (2015), Shim et al. (2013); COSMOS from Civano et al. (2016), Marchesi et al. (2016); GOODS-N from Xue et al. (2016); EGS from Nandra et al. (2015); CDFS from Luo et al. (2016); E-C
(2006), Silverman et al. (2010), Treister et al. (2009); UDS from Ueda et al. (2008), Akiyama et al. (201

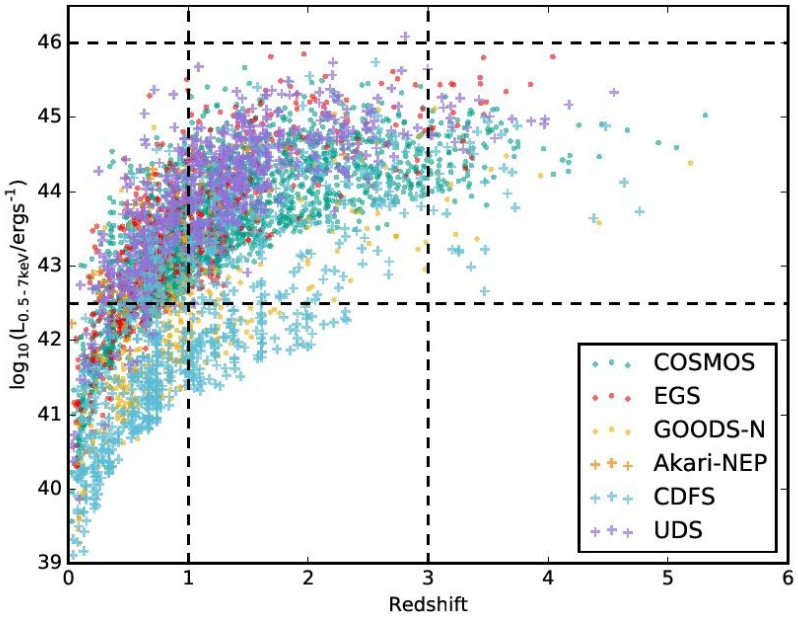

От большинства рентгеновских источников сигнала в субмиллиметрах нет!

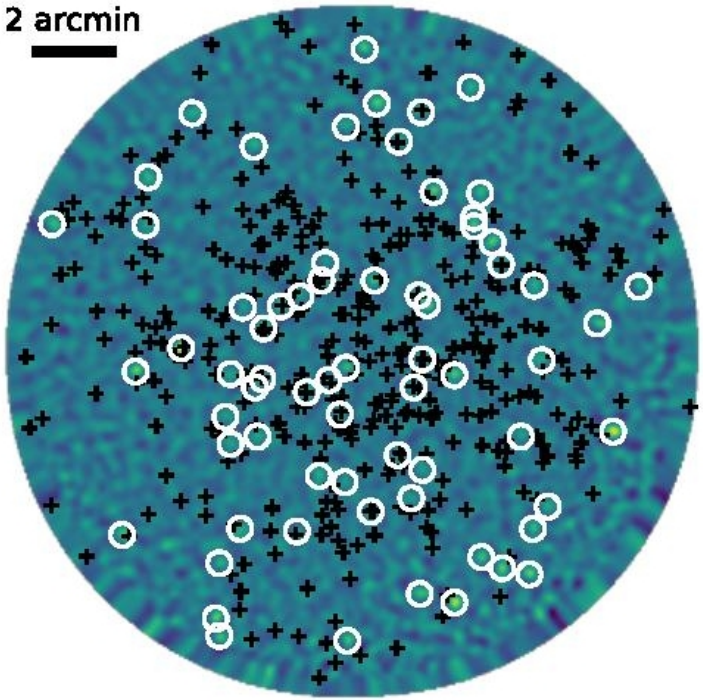

Figure 3. The S2CLS map of the GOODS-N field. Submillimetre detections from the S2CLS catalogue (>3.5 σ) are marked with white circles, and X-ray detections are marked with black crosses. Where there are two X-ray sources within the matching radius of an S2CLS source, the nearest match is assumed to be the correct counterpart. The majority of X-ray sources are not detected at 850 μm at the 3.5 σ level.

Поэтому все поскладывали

Table 4. Stacked 850 μm flux in each of four L_X bins. Column 1 shows the name of the bin, column 2 the range of X-ray luminosities, column 3 shows the number of sources in each bin and column 4 shows the 850 μm median stacked flux in mJy.

L_X bin	L_X range (10^{43} erg s^{-1})	no. sources	median flux (mJy)	mean flux (mJy)
L1	0.351 – 3.48	359	$0.30^{+0.22}_{-0.12}$	$0.45^{+0.11}_{-0.04}$
L2	3.48 – 9.55	389	$0.53^{+0.24}_{-0.30}$	$0.63^{+0.11}_{-0.04}$
L3	9.55 – 26.6	414	$0.50^{+0.23}_{-0.19}$	$0.67^{+0.11}_{-0.04}$
L4	26.6 – 710.	474	$0.48^{+0.22}_{-0.15}$	$0.61^{+0.09}_{-0.03}$

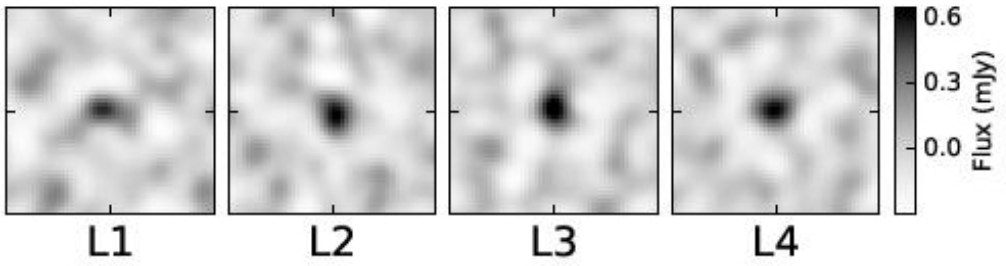

Figure 7. Median stacked images for each L_X bin (see Table 4). Each image is 100 × 100 arcsec.

Поэтому все поскладывали

Table 2. Number of X-ray sources, and those with submillimetre detections, in each L_X bin. Column 1 shows the range in L_X of each bin, column 2 shows the number of sources, column 3 shows the number of 850 μm detections, column 4 shows the detection fraction as a percentage, and column 5 shows the median redshift in each bin.

$\log L_X$(erg s^{-1})	no. sources	850 μm?	%	z_m
42.5 – 43.4	321	7	2.18	1.19
43.4 – 44.3	865	21	2.43	1.45
44.3 – 45.1	692	9	1.30	1.80
45.1 – 46	79	2	2.53	2.05

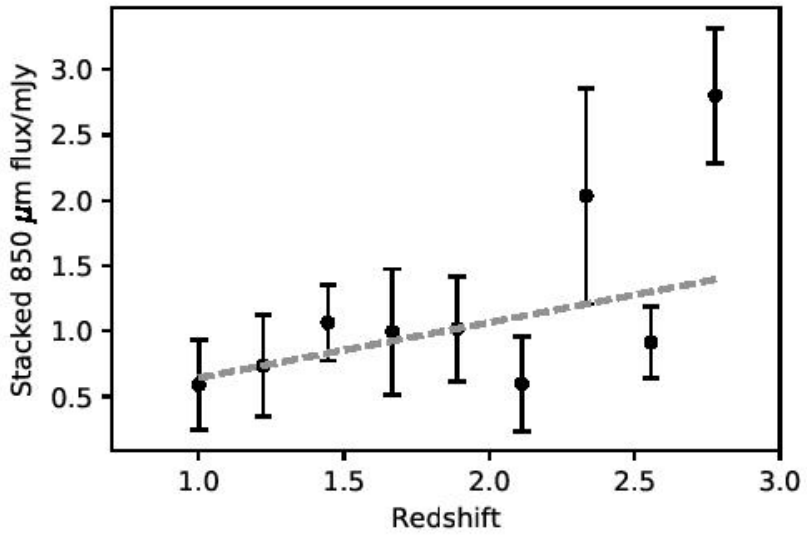

Figure 5. Stacked 850 μm flux with redshift. The dashed line shows a weighted least squares fit to the data points, which gives a slope of 0.42; errorbars show 1-σ uncertainties on the stacked fluxes.

… и в других длинах волн тоже

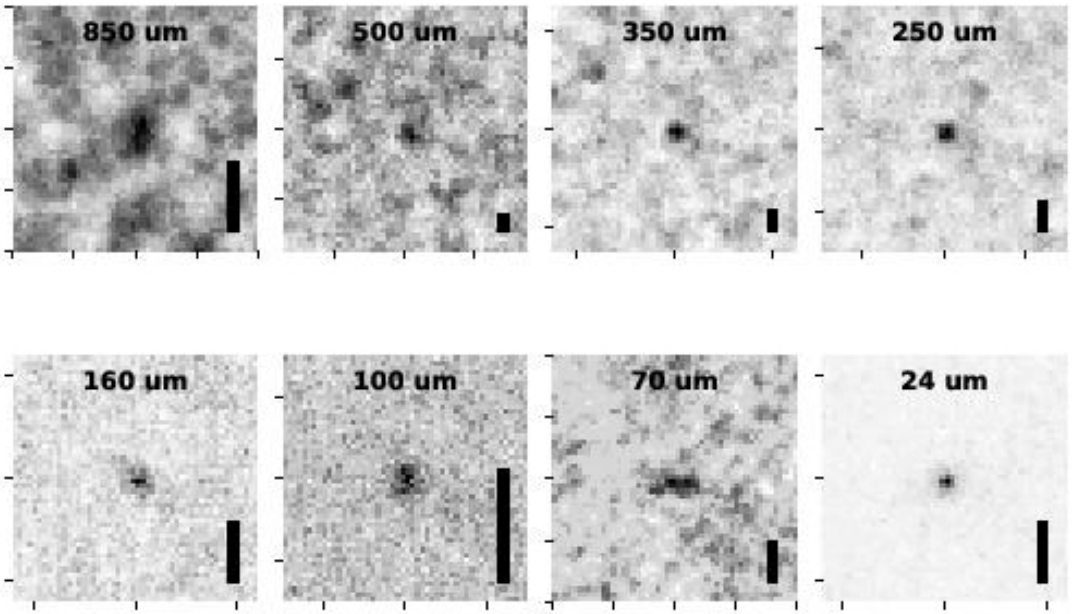

Figure 9. Example stacked images in each wavelength. The black bar on each image indicates 25 arcsec scale.

… и вписали SED – двухкомпонентный

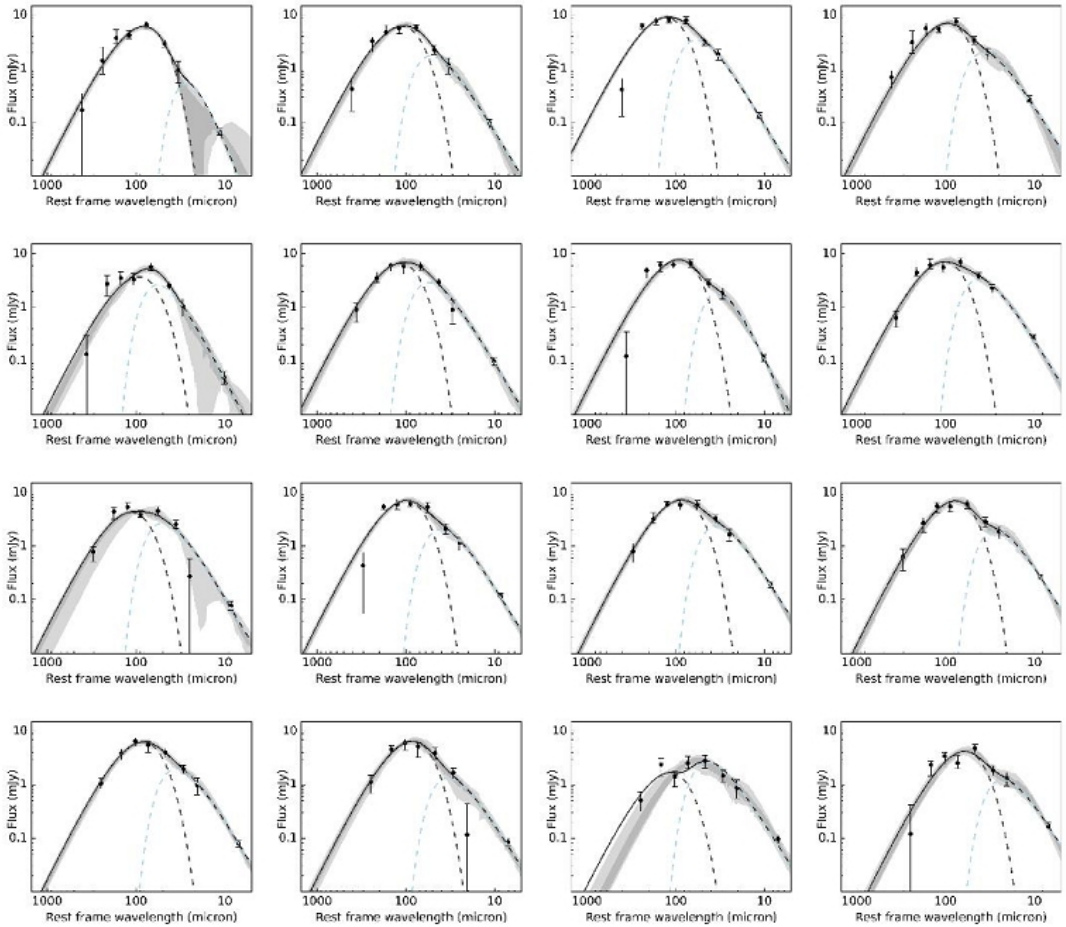

Figure 10. SED fits for each of the 16 'average' sources. Median stacked fluxes are shown as black points, with associated 1σ errors

Результаты

Table 5. Median properties of each of the 16 bins in redshift and X-ray luminosity. Column 1 shows the redshift range of each bin, column 2 shows the number of sources, column 3 the median redshift, column 4 the median X-ray luminosity in erg s^{-1}, and column 5 the calculated SFR in solar masses per year, as described in section 3.5.

z-range	No. sources	z_m	L_X (10^{43} erg s^{-1})	SFR ($M_\odot$ yr^{-1})
1 – 1.24	93	1.10	1.12	85^{+8}_{-5}
	92	1.10	2.55	77^{+5}_{-12}
	92	1.14	5.95	79^{+9}_{-5}
	93	1.09	20.7	100^{+7}_{-14}
1.24 – 1.53	89	1.32	1.87	144^{+18}_{-25}
	88	1.38	3.84	122^{+24}_{-22}
	88	1.33	10.5	167^{+11}_{-28}
	89	1.40	31.7	137^{+31}_{-12}
1.53 – 2.05	87	1.76	3.70	155^{+18}_{-23}
	86	1.76	7.37	299^{+18}_{-43}
	86	1.80	19.3	351^{+29}_{-64}
	87	1.88	50.4	366^{+49}_{-37}
2.05 – 3	87	2.47	7.46	592^{+95}_{-50}
	86	2.53	15.6	600^{+141}_{-62}
	86	2.39	30.0	453^{+71}_{-157}
	87	2.45	110	588^{+114}_{-54}

Как и в более ранних работах, темпы SF НЕ зависят от активности AGN

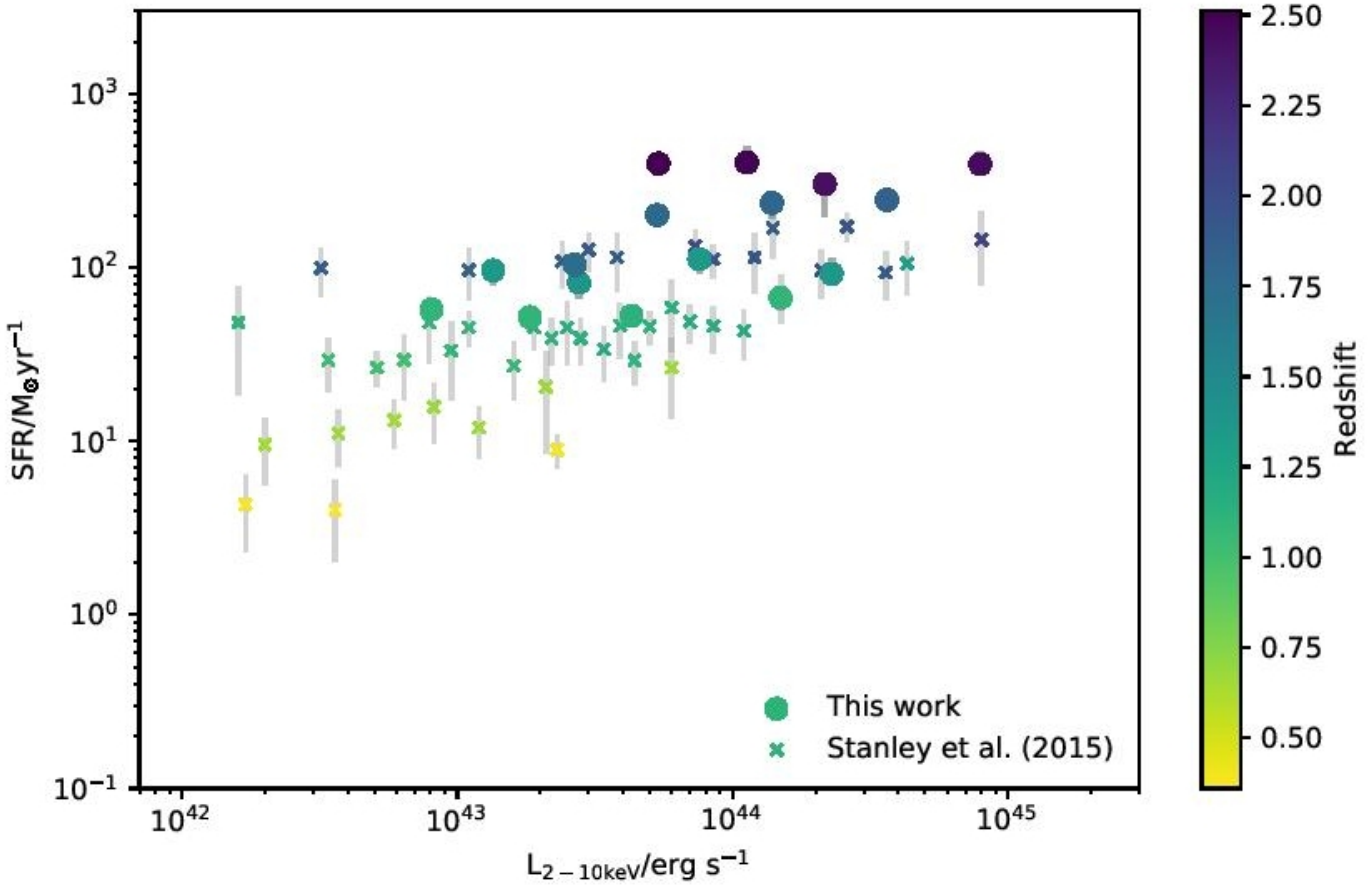

… но так и должно быть! (Сравнение с симуляциями)

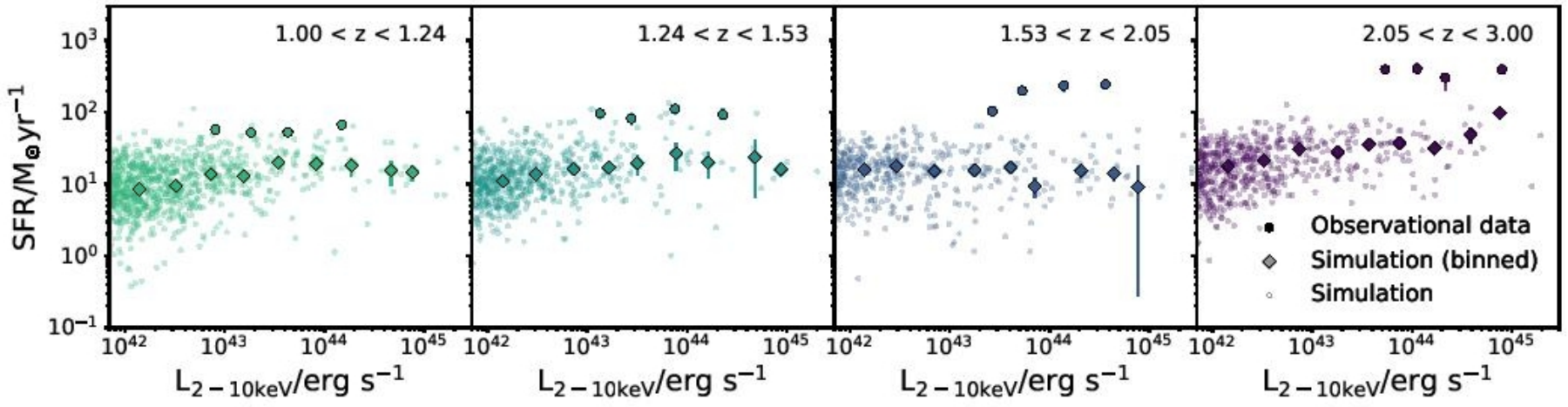

Figure 12. SFR versus X-ray luminosity, for both the observational data (filled circles) and the simulated HORIZON-AGN galaxies (dots, with binned values shown with filled diamonds), for each redshift bin. Colours correspond to redshifts in Fig. 11. Both observations and simulations show, within each redshift bin and across this L_X range, a flat trend of SFR with increasing L_X.